

Characterizing and Mitigating Digital Sampling Effects on the CYGNSS Level 1 Calibration

Scott Gleason, *Senior Member, IEEE*, Mohammad M. Al-Khaldi, *Member, IEEE*, Christopher Ruf, *Fellow, IEEE*, Darren S. McKague, *Member, IEEE*, Tianlin Wang, *Member, IEEE*, Anthony Russel

Abstract—This paper presents a detailed examination of fluctuating input noise power levels on the analog to digital converter (ADC) sampling hardware of the NASA CYGNSS instruments and the associated impacts on the level 1 NBRCS estimation performance. The impact of external noise variations on both the CYGNSS science and navigation channels are quantified with respect to how the fluctuating received power impacts the low level ADC sampling distribution and subsequent NBRCS estimation. This work demonstrates that there are clear quantifiable geo-spatially dependent noise variations linked to GNSS space based augmentation systems (notably QZSS and WAAS) and that these additional noise sources significantly alter the digital sampling distribution of the CYGNSS instruments, actively degrading the level 1 NBRCS estimation if not corrected. A derivation of the theoretical correction for both the science and navigation channel ADC sampling variations is presented which is later tuned based on empirical performance metrics in an effort to minimize the induced calibration errors. The impacts of the enhancements outlined in this work on CYGNSS level 1 calibration are evaluated using 1 year of observations before and after the digital sampling corrections, using model ECMWF wind and Wavewatch III MSS surface validation data sets.

Index Terms—Calibration, GNSS, GPS, Reflectometry, Bistatic Radar, CYGNSS

I. INTRODUCTION AND BACKGROUND

GLOBAL Navigation Satellite System (GNSS) Reflectometry (GNSS-R) consists of measuring bistatic surface reflections from GNSS transmitters for the purpose of Earth remote sensing.[1], [2], [3].

A number of advantages of GNSS-R are achieved through their L-band operating frequencies which provide reasonable penetration through thick vegetation canopies, insensitivity to heavy rain and cloud cover. Practically, the passive nature of the instruments which act as receivers of navigation signals

Corresponding author: Scott Gleason.

Scott Gleason and Mohammad M. Al-Khaldi are with the Constellation Observing System for Meteorology, Ionosphere, and Climate (COSMIC) Program, University Corporation for Atmospheric Research (UCAR), Boulder, CO 80301 USA. (email: gleason@ucar.edu, malkhaldi@ucar.edu).

Christopher Ruf is with the Department of Climate and Space Sciences and Engineering, University of Michigan, Ann Arbor, MI 48109 USA, and also with the Department of Electrical Engineering and Computer Science, University of Michigan, Ann Arbor, MI 48109 USA (e-mail: cruf@umich.edu).

Darren S. McKague is with the Department of Climate and Space Sciences and Engineering, University of Michigan, Ann Arbor, MI 48109 USA (e-mail: dmckague@umich.edu).

Tianlin Wang is with the Department of Electrical and Computer Engineering and ElectroScience Laboratory, The Ohio State University, Columbus, OH 43210 USA. (e-mail: wang.15085@osu.edu).

Anthony Russel is with the Space Physics Research Laboratory, University of Michigan, Ann Arbor, MI 48109 USA (e-mail: russelan@umich.edu).

Manuscript received July 2021

of opportunity can be achieved at relatively low-cost using commercially available materials with their short procurement times. This allows for the design and launch of multiple receiver constellations which can achieve superior spatial and temporal coverage, compared to single satellite missions. These factors have contributed considerable to the proliferation of GNSS-R measurements for a variety of applications including soil moisture retrieval [4], [5], [6], [7], biomass estimation [8] and inland water body mapping [9], [10], [11], [12], [13], [14] and ocean surface altimetry [15]. Additionally, these systems continue to play an increasing role in remote sensing of the ocean wind and waves [16], [17], [18], [19] and improving hurricane forecasting [20], [21], [22] where the relationship between the forward scattered GNSS signals and ocean conditions can be retrieved based on well established physical relationships between surface winds, ocean surface roughness and the incoherent surface scatter [23], [24].

An example of this is NASA's 2016 Earth Venture constellation of 8 Low Earth Orbit (LEO) receivers, the Cyclone Global Navigation Satellite System (CYGNSS) mission [25], each hosting a primary delay-Doppler Mapping Instrument (DDMI) [26] payload enabling the constellation's use for GNSS-R Earth remote sensing. The operation of the CYGNSS receivers is that of a spaceborne passive radar system with each the constellation's eight observatories forming a specular bistatic geometry together with a GPS transmitter whose Earth reflected L1 C/A codes are received by either of the observatories two nadir science antennas, port and starboard, and cross-correlated with local code replicas. The different forward paths associated with received surface scatter give rise to delay diversity while the motions of the receiver, transmitter and reflecting surface lead to Doppler diversity such that the received surface scatter is mapped from the spatial domain to delay-Doppler space giving rise to the fundamental GNSS-R measurement, the delay-Doppler Map (DDM). CYGNSS's standard Level-1 DDMs span 17 delay bins (with $\approx 0.25\mu\text{s}$ per-pixel sampling) and 11 Doppler bins (with ≈ 500 Hz, per-pixel sampling).

The individual CYGNSS instruments each contain 4 parallel channels, with each channel capable of tracking a single surface reflection. Combined, the 8 CYGNSS satellites, each tracking 4 observations in parallel, are capable of a total of 32 DDMs per processing interval (initially configured at 1 second, then commanded to a shorter 0.5 second in 2019 to improve along track surface resolution). These level 0 observations are initially computed in uncalibrated units of raw counts. To derive the observable of most relevance for the mission's

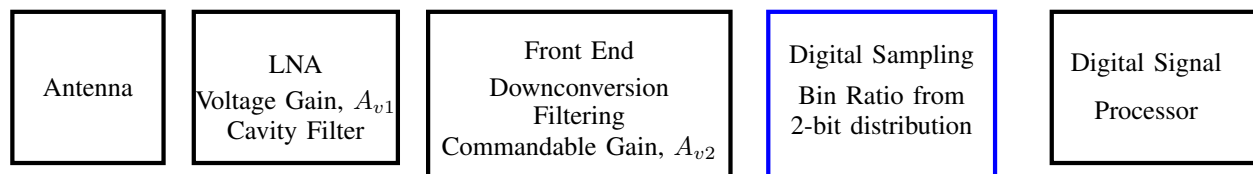


Fig. 1. Analog to digital signal processing chain (left to right) of CYGNSS instrument. Analog signal is digitally sampled after a commandable voltage gain (A_{v2}) in the instrument front end electronics.

core objectives, the Normalized Bistatic Radar Cross Section (NBRCS), a smaller cropping window is used to integrate surface scatter within ± 1 delay pixels and ± 2 Doppler pixels about the specular bin to form the delay-Doppler Map Average (DDMA) that is normalized by an estimate of effective scattering areas to form the CYGNSS NBRCS. This process is preceded by two levels of calibration, ‘L1A’ and ‘L1B’, that aim to convert the initial ‘Level-0’ DDMs from their units of raw counts to power Level-1 DDMs in units of watts and later to bistatic radar cross section (BRCS) DDMs in units of m^2 , respectively, through accounting for a variety of instrument and reflection-geometry related factors. This includes accounting for transmitter effective isotropic radiated power (EIRP) which has recently been shown to be highly dynamic thereby necessitating its direct tracking through each of the eight observatories’ zenith antennas [27], [28], receivers’ antenna gains, signal forward paths’ ranges, low noise amplifier (LNA) temperature, instrument gain and fluctuating observations of noise levels. For a more comprehensive overview see [29].

While the accurate estimation of all of the aforementioned calibration parameters is crucial for the successful calibration of CYGNSS data and its subsequent use for science applications, this paper is primarily concerned with providing a comprehensive analysis of the latter term; presenting an examination of the dynamic external noise environment the eight satellite constellation operates in, its effects on input noise power levels and the cascading effects this may have on Level-1 calibration if not adequately accounted for.

On-orbit GNSS-R measurements both from the CYGNSS mission and the TechDemoSat-1 (TDS-1, [30]) satellite showed significant global spatial variation in the received observation noise floors, previously presented in [31] and [32], respectively. It was believed that this was due to both: a) natural external antenna noise fluctuations and, b) nuisance signal reflections from other GNSS systems, notably from GNSS Space Based Augmentation Systems (SBAS) [33], [34], [35]. These results demonstrated that transmissions from other GNSS satellites (those not used to perform the GNSS-R remote sensing measurement) can significantly alter the observation noise. In the case of CYGNSS, the observed noise is used directly in the level 1 calibration, and as we will show in this analysis, uncertainty in the noise level can introduce significant errors in the NBRCS estimates.

The next Section provides an overview of the ADC sampling design of the CYGNSS instrument and identifies key terms used in subsequent analysis. Section III presents a summary of the magnitude and spatial distribution of on-orbit observed CYGNSS noise, highlighting regional anomalies

in uncorrected noise floor estimates and their impacts on CYGNSS’s ADC sampling hardware. These effects are further explored in Section IV, presenting a quantitative assessment of the errors introduced to the level 1 CYGNSS NBRCS estimates and a theoretical correction (with minor empirical tuning) to the CYGNSS science observation noise levels. Section V performs an analysis and correction for digital sampling errors on the CYGNSS direct channel GPS effective isotropic radiated power (EIRP) estimates used in the level 1 calibration. Section VI presents a before and after error assessment of the corrected CYGNSS level 1 NBRCS data products. Section VII includes a summary and discussion of the results.

II. OVERVIEW OF ANALOG TO DIGITAL SAMPLING DESIGN OF CYGNSS INSTRUMENT

This paper focuses solely on the specific details of the CYGNSS instrument digital sampling design and does not consider alternative sampling strategies. For a more information on the general theories underlying analog to digital sampling strategies additional reference sources should be consulted, such as [36] or for the specific case of GNSS receivers [37].

A. Analog to Digital Sampling of Input Noise Levels

The CYGNSS instrument input signal processing chain is illustrated in Figure 1. After capture of the off-air signal by the receive antenna, the signal enters the LNA and is processed through a cavity filter and initial fixed voltage gain stage A_{v1} . Following this initial amplification stage, the received signal travels to the instrument front end where additional down-conversion and filtering is applied. This includes added amplification by a commandable voltage gain A_{v2} which permits adjustment of the analog signal level into the ADC. It is noted, that numerous GPS receivers configure the front end into an Automatic Gain Control (AGC) mode in order to autonomously adjust A_{v2} , thereby securing an ideal Normal sampling distribution (See Figure 2). However, the need for knowledge of the precise input power level for a science observation prohibits this convenience, and necessitates that G_2 remains at a constant commanded value for the CYGNSS receivers.

The need to manually command the front end gain settings, adds the requirement that the input signal levels be compatible with the 2-bit ADC digital sampling thresholds (which are fixed within the front end), at states ± 1 and ± 3 in the case of CYGNSS. This is demonstrated in Figure 2 for three cases. The left column shows an example G_2 which is too high

(increased magnitude of real analog voltage samples). In this case, the sampled input signal falls disproportionately into bin 1 (below lower threshold) and bin 4 (above high threshold). This results in a non-ideal inverted sampling distribution as shown directly below.

Alternatively, if G_2 is commanded too low (shown in the right column) the sampling shifts to bin 2 and bin 3 (on either side of the zero voltage reference), and results in a peaked sampling distribution. Ideally, G_2 should be commanded to a level which results in a near-ideal Normal (Gaussian) sampling distribution of the 4 bins, as shown in the center column.

As the sampling distribution deviates from the Normal (Gaussian) shape, a small and gradual degradation in the downstream processed retrieved signal power levels arises [38]. It is important to note that GNSS signals when sampled off-air are typically at levels well below the input noise floor [39] and are subsequently detected using a coherent (spread spectrum) processing technique [40] in the digital signal processor such that the sampling distribution in a GNSS receiver is driven mostly by the input noise level (directly linked to the cascaded system gain $A_{v1} + A_{v2}$).

III. CHARACTERIZATION OF CYGNSS ON-ORBIT DIGITAL SAMPLING PERFORMANCE

A. Sampling Distributions of CYGNSS Satellites

It is convenient to define a single metric to quantify the digital sampling distribution. We have chosen to do this in a parameter called the Bin Ratio (BR), which is defined as,

$$BR = \frac{b2 + b3}{b1 + b4} \quad (1)$$

where, $b1, b2, b3, b4$ are, respectively, the number of counts accumulated into each of the four digital sampling bins, -3, -1, +1 and +3 respectively over a short time interval (see Figure 2 for a simulated illustration of the four sampling bin behavior) that in the case of the CYGNSS receivers is 1 second. In reference to Figure 2, the bin ratio for the inverted distribution (left) is $BR = 0.62$, for the Normal/Gaussian distribution (center) is $BR = 2.15$, and for the peaked distribution $BR = 4.52$. The low and high BR examples present limiting scenarios for illustration.

The bin ratio distributions for each of the eight CYGNSS observatories' starboard, port and zenith antennas as observed on-orbit are shown in Figure 3, with statistics summarized in Table I. The observed ranges of the CYGNSS instruments generally fall between slightly below 1.00 to slightly above 2.15, which is a (non-ideal) but acceptable range.

Discussion of CYGNSS Bin Ratio Distributions: The statistics summarized in Table I make clear that the CYGNSS input channels are associated with non-ideal BR distribution, all having means \overline{BR} below the 2.15 value corresponding to a Gaussian distribution. This is expected to be an artifact of the initial commanded front end gain settings being slightly higher than the value that ensures an optimal BR distribution, but nonetheless still at acceptable levels for remote sensing applications (as indicated by wind speed retrievals from

Param./FM	1	2	3	4	5	6	7	8
Star. \overline{BR}	1.14	1.58	1.66	1.53	1.68	1.31	1.55	1.82
Star. $\sigma(BR)$	0.20	0.27	0.29	0.29	0.23	0.22	0.26	0.31
Port \overline{BR}	1.49	1.34	1.11	1.66	1.47	1.40	1.46	1.56
Port $\sigma(BR)$	0.29	0.25	0.19	0.32	0.29	0.23	0.21	0.26
Zen. \overline{BR}	1.17	0.99	1.64	1.01	1.64	1.35	1.25	1.16
Zen. $\sigma(BR)$	0.10	0.09	0.14	0.08	0.16	0.09	0.11	0.09

TABLE I
SUMMARY OF CYGNSS BIN RATIO DISTRIBUTIONS ACROSS ALL OBSERVATORIES AND INPUT CHANNELS. \overline{BR} DENOTES A BIN RATIO MEAN AND $\sigma(BR)$ DENOTES A BIN RATIO STANDARD DEVIATION.

CYGNSS that meet mission requirements [41]). There are two potential problems with the current CYGNSS front end gain configuration, should the BR distribution become too extreme (i.e. vary significantly from Gaussian, to levels below 1.0 or above 3.0, for example); a) the 2-bit digital sampling distribution starts encroaching towards a 1-bit sampling configuration which results in known captured signal power losses [37], and b) as will be demonstrated below, the further the bin ratio from nominal the larger the (non-linear) correction needs to be to standardize the input to a common reference, which can potentially introduce increased calibration uncertainty.

As the bin ratio falls below 1.00, the corrections become more severe, which motivates the re-commanding of new values of G_2 for instrument channels with lower distribution means. It is the long term goal of the CYGNSS mission to adjust these marginally low BR channels to shift the distribution upward towards the nominal reference. In fact, this on-orbit operation was performed for the CYGNSS FM 3 port channel in late 2020, resulting in a notable shift up toward nominal levels. However, these adjustments, often cause subtly and unduly large shifts in the downstream NBRCS distributions and ocean wind speed retrievals and have the potential to degrade legacy version of the CYGNSS level 1 calibration and wind speed retrievals beyond acceptable bounds. Therefore, as this proposed ADC correction is integrated into future CYGNSS level 1 calibration versions and downstream bias corrections are recalculated, it is expected that on-orbit gain adjustments to the out-of-family input channels (i.e. CYG01 and CYG06 starboard channels in addition to CYG03 port channel) will be rolled out.

B. Observed Noise Fluctuations in CYGNSS Observations

The presence of external noise fluctuations on CYGNSS observations was initially presented in [31] where correlation between the received on-orbit noise levels and observation geometries that resulted in SBAS satellite reflections in the CYGNSS science antenna main beams was established. Both the U.S. Wide Area Augmentation System (WAAS) and the Japanese Quasi-Zenith Satellite System (QZSS) exhibited noticeably significant impacts (note the low BR mean in the region of Japan due to QZSS, as well as low BR in the north and south Pacific due to WAAS in Figure 4).

The satellites of the GPS SBAS constellations use distinct pseudo-random noise (PRN) codes for each transmitter, and the correlation of two distinct L1 Coarse/Acquisition (C/A)

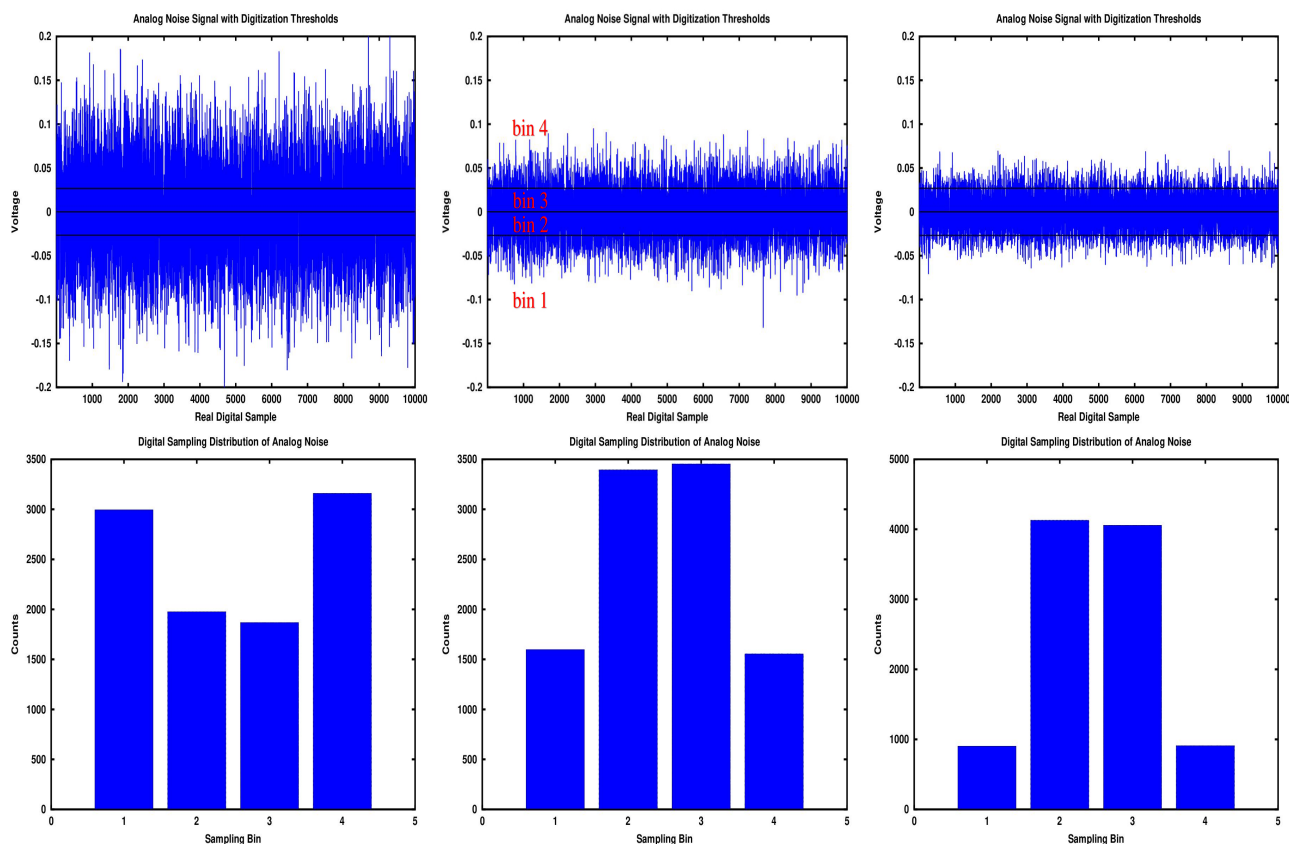


Fig. 2. Simulated examples of short time sequences of analog noise voltage with respect to digital sampling thresholds and their resulting digital sampling distributions. (Left Column) for an analog signal strength that is too high for the given gain setting (inverted distribution); (Middle Column) for an ideal balance between signal strength and gain setting, resulting in a bin ratio of 2.15; and (Right Column) for a signal strength that is too low for the given gain setting (peaked distribution).

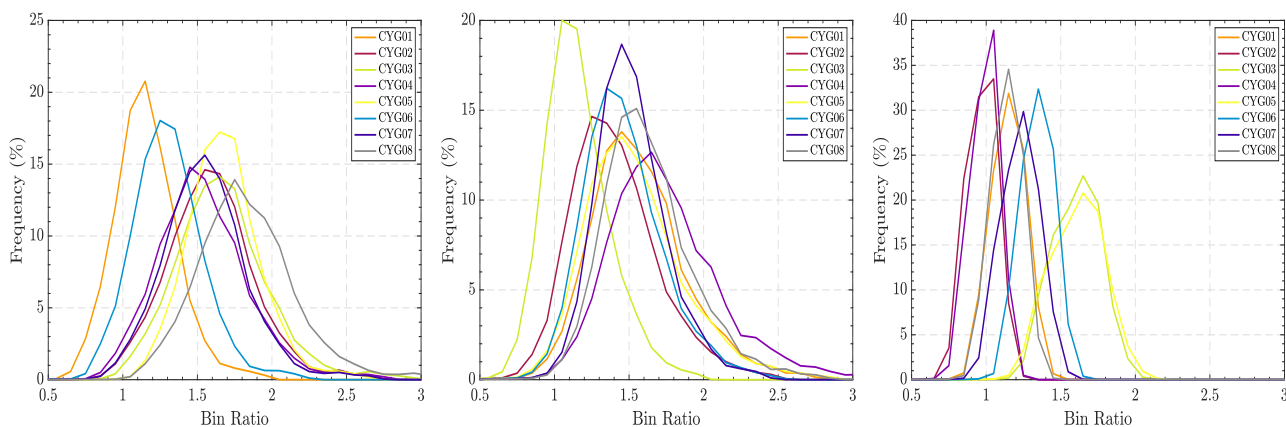


Fig. 3. CYGNSS on-orbit bin ratio distributions for (left) the ocean observations of the starboard input science channels and (center) the port input science channels. (right) All observations on the zenith navigation channels for all eight CYGNSS observatories.

PRN codes results in a power level that appears similar to a noise contribution that is approximately 24 dB lower than the correlated “signal” obtained from the auto-correlation of a code with itself [37]. The close co-existence in frequency of a large number of GNSS transmissions is believed to be the underlying cause of the noise floor fluctuations. Regardless, Figure 4 illustrates the potential of significant regional calibration and wind speed retrieval errors if the variable noise power levels incident on the instrument digitiser are not corrected.

IV. IMPACT OF BIN RATIO VARIATIONS ON SCIENCE OBSERVATIONS AND PROPOSED CORRECTION

To demonstrate the impact of fluctuating bin ratio on the primary CYGNSS level 1 (NBRCS) and Level 2 (wind speed) products, a 1-year long CYGNSS data record was analyzed across all observatories for both port and starboard science channels.

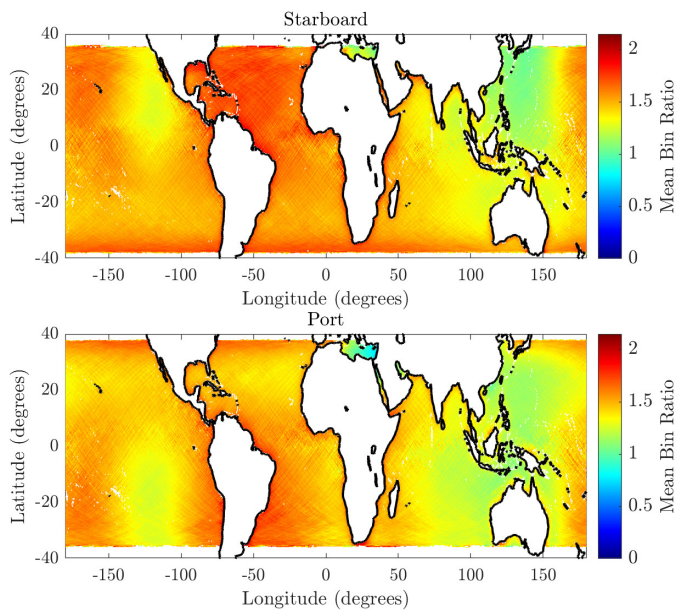


Fig. 4. CYGNSS on-orbit geospatial bin ratio distributions for (top) starboard input science channels and (bottom) port input science channels. The regions of low BR in both antenna orientations correspond to increased noise levels due to SBAS reflections (primarily QZSS and WAAS).

A. Quantifying Bin Ratio Induced Errors on NBRCS

Figure 5 illustrates the positive correlation of NBRCS and BR over a full year year of CYGNSS data (2019). Bin ratio estimates over this year long data record are computed using Equation 1 and the NBRCS is the mean value across all CYGNSS observatories within narrow $\Delta BR = 0.05$ bins. The surface MSS and wind speed reference data are based on temporal and spatial match-ups from ECMWF ocean surface wind speed (in 0.25 m/s bins).

It is important to note that there is some uncertainty in the ECMWF model wind speed estimates which will couple into this analysis. However, it is believed that ECMWF re-analysis winds are a reasonably reliable reference source and suitable for this application. The estimated uncertainty in the ECMWF winds has been estimated to be on order of 0.5 m/s RMSE globally [42], [43].

Additionally, WaveWatch III (WW3) wave mean square slope model [44] has been used as a surface reference. To account for the CYGNSS observation frequency, an L-band adjusted spectral tail ([45], [46]) has been applied to the WW3 outputs and the surface isolated over narrow MSS conditions (in 0.0005 width bins). The accuracy of this L-band spectral tail corrected model MSS is unknown and the subject of ongoing research. Yet, these data provide a more direct surface link to the CYGNSS L-band observations than the near surface wind speeds and are included as a secondary comparison source.

In the idealized scenario of no calibration errors or uncertainties, NBRCS estimates should be independent of all instrument quantities with no correlation to bin ratios. The clear correlation of NBRCS on BR present however, makes clear the effects of SBAS driven fluctuating input noise power levels on CYGNSS ADCs and how this may compromise the

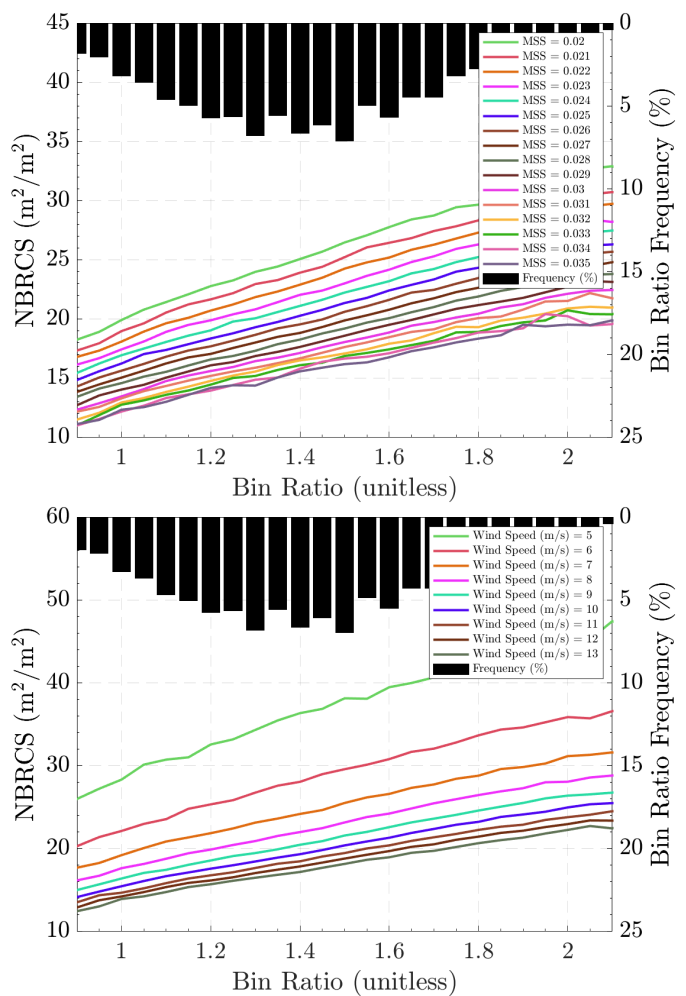


Fig. 5. Mean NBRCS estimates vs science channel bin ratio for a wide range of ocean conditions without digital sampling correction. (Above) Over a range of surface MSS conditions (ref. WW3) and (Below) over a range of wind conditions (ref. ECMWF)

accuracy of the constellation’s level 1 calibration if not accounted for in the CYGNSS wind speed estimation algorithms that rely on NBRCS in their retrievals [47], [48]. The examples summarized in Figure 5 demonstrate the need for a digital sampling correction based on the observed BR .

B. Theoretical Digital Noise Floor Correction

The input noise power is the dominant component of the pre-correlated GPS signal received at the instrument ADC converter. Thus, a correction to the observed noise floor can be performed to mitigate received power uncertainty due to BR fluctuations driven largely by external noise variations. The steps for generating a theoretical noise floor correction function are outlined in Figure 6.

The correction is designed as an adjustment to the per-observation estimated CYGNSS level 0 noise counts. The received signal power counts in the CYGNSS level 1 calibration are estimated after subtraction of the estimated noise floor C_N ([29], [49]); that is the difference of the total counts (C) and noise counts: $C - C_N$. As a result, by correcting the noise counts, we are directly adjusting the downstream estimated

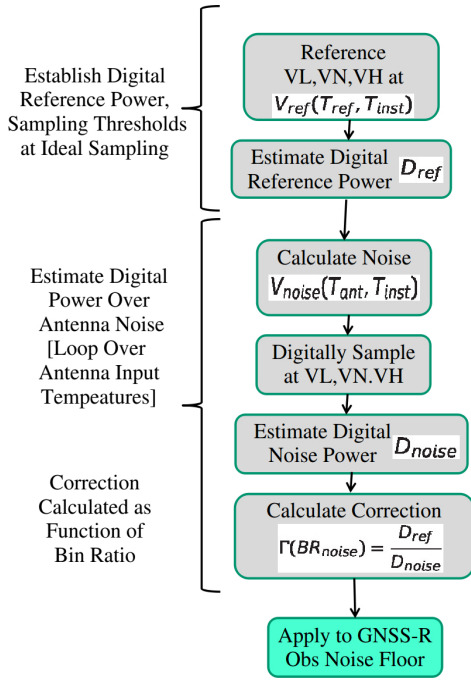


Fig. 6. Summary of steps in the generation of the theoretical noise floor correction.

Parameter	Value	Comment
BW	2e6 Hz	Inst. Bandwidth
Z_0	50 ohms	Inst. Impedance
A_v	46 dB	Total Inst. Voltage Gain
NF	2.5 dB	Inst. noise figure
T_{ref}	99.4 K	Reference Temperature
T_{ant}	40 to 400 K	Antenna Temperature
μ	0	Noise Distribution Mean
σ	Calculated	Noise RMS Voltage

TABLE II

CYGNSS INSTRUMENT PARAMETERS USED IN DERIVING NOISE FLOOR CORRECTION.

level 1 power levels, including the normalized bistatic cross section (NBRCS) estimate.

Table II contains the CYGNSS instrument assumptions used during the correction derivation.

As per Figure 6: Initially, an ideal digitally sampled reference power is estimated. The reference instrument temperature is calculated from the reference instrument noise figure (NF) as,

$$T_{inst} = (NF - 1)290 \quad (2)$$

which is then added to the antenna reference temperature (T_{ref}), and used to calculate the reference power,

$$P_{ref} = k(T_{ref} + T_{inst})BW \quad (3)$$

Next, the reference power level is converted to the voltage level received at the instrument ADC converter using the instrument cascaded voltage gain and characteristic impedance,

$$V_{ref} = A_v \sqrt{P_{ref} Z_0} \quad (4)$$

where, $V_{ref} = \sigma_{ref}$ results in a Normal voltage distribution with zero mean. The reference voltage PDF is given by (5).

$$n_{ref}(x) = \frac{1}{2\pi\sigma_{ref}} \exp \frac{-x}{2\sigma_{ref}^2} \quad (5)$$

Next, the reference sampling thresholds are computed using the 1-sigma reference voltages such that,

$$V_L = -V_{ref}, V_N = 0, V_H = V_{ref} \quad (6)$$

The bin counts b_1, b_2, b_3, b_4 for the input reference noise level can be obtained by integrating the cumulative distributions of a set of noise samples based on the reference ADC sampling thresholds (V_L, V_N, V_H) set at the reference noise level (generated at V_{ref}), as follows,

$$b_{1ref} = \int_{-\infty}^{V_L} n_{ref}(x) dx \quad (7)$$

$$b_{2ref} = \int_{V_L}^{V_N} n_{ref}(x) dx \quad (8)$$

$$b_{3ref} = \int_{V_N}^{V_H} n_{ref}(x) dx \quad (9)$$

$$b_{4ref} = \int_{V_H}^{\infty} n_{ref}(x) dx \quad (10)$$

Thus, the digital sampled input power reference at the ideal 2-bit sampling $BR = 2.15$ can be estimated using Cooper 2-bit weights [50] as (11).

$$D_{ref} = 9(b_{1ref} + b_{4ref}) + (b_{2ref} + b_{3ref}) \quad (11)$$

Subsequently, by varying the input antenna noise temperature (T_{ant}), and the associated real sampled noise voltage levels, we can quantify the changes in the digitally sampled input power levels received over a full range of external antenna noise conditions. The corresponding terms for the input noise power and voltage over variable external antenna noise levels can be expressed as,

$$P_{noise} = k(T_{ant} + T_{inst})BW \quad (12)$$

$$V_{noise} = A_v \sqrt{P_{noise} Z_0} \quad (13)$$

where T_{ant} covers a range of input noise temperatures (see Figure 6, Table II). V_{noise} is the noise voltage standard deviation (σ_{noise}) at the variable input noise power levels. The variable input signals will exhibit Normal distributions as per the examples shown in Figure 2, and expressed as,

$$n_{noise}(x) = \frac{1}{2\pi\sigma_{noise}} \exp \frac{-x}{2\sigma_{noise}^2} \quad (14)$$

The input noise is then digitized at the **reference voltage levels** (Equation 6), resulting in a 2-bit digital sample distribution expressed as,

$$b_{1noise} = \int_{-\infty}^{V_L} n_{noise}(x) dx \quad (15)$$

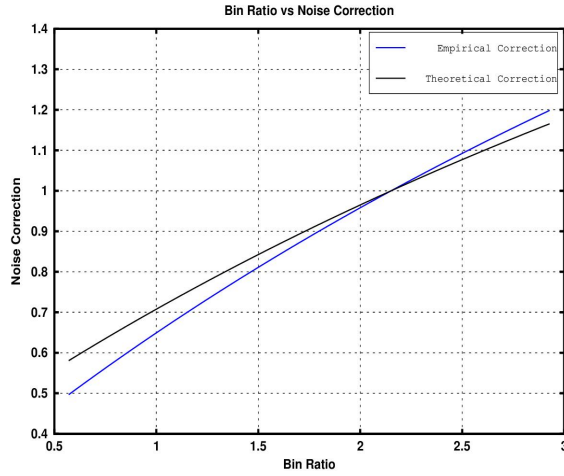


Fig. 7. Theoretical and empirically adjusted digital sampling noise floor corrections applied to CYGNSS v3.1 level 0 noise levels.

$$b_{2noise} = \int_{V_L}^{V_N} n_{noise}(x)dx \quad (16)$$

$$b_{3noise} = \int_{V_N}^{V_H} n_{noise}(x)dx \quad (17)$$

$$b_{4noise} = \int_{V_H}^{\infty} n_{noise}(x)dx \quad (18)$$

The resulting bin ratio (BR) and the two bit digital power at the variable input noise levels are calculated as,

$$BR_{noise} = \frac{b_{2noise} + b_{3noise}}{b_{1noise} + b_{4noise}} \quad (19)$$

$$D_{noise} = 9(b_{1noise} + b_{4noise}) + (b_{2noise} + b_{3noise}) \quad (20)$$

Finally, the noise floor vs BR correction (Γ) is calculated as the ratio between the reference digitally sampled power and the resulting sampled power in the presence of external noise,

$$\Gamma_{ref}(BR_{noise}) = \frac{D_{ref}}{D_{noise}} \quad (21)$$

This correction is applied to CYGNSS level 0 noise counts for each observation during the standard level 1 calibration procedure. The resulting bin ratio noise floor correction curve is shown in Figure 7.

Importantly, errors in the instrument assumptions in Table II do not impact the resulting correction curve as the reference and variable noise input functions pass through the same hardware channel. Therefore, instrument hardware parameter contributions cancel at the point of taking the correction power ratio as in (21).

C. Empirical Optimization of Theoretical Correction

Upon application of the derived correction (Eq. (21) and Figure 7), it was observed that the results could be improved slightly by adding a small multiplicative scaling factor to the theoretical correction. With the final noise floor correction applied being,

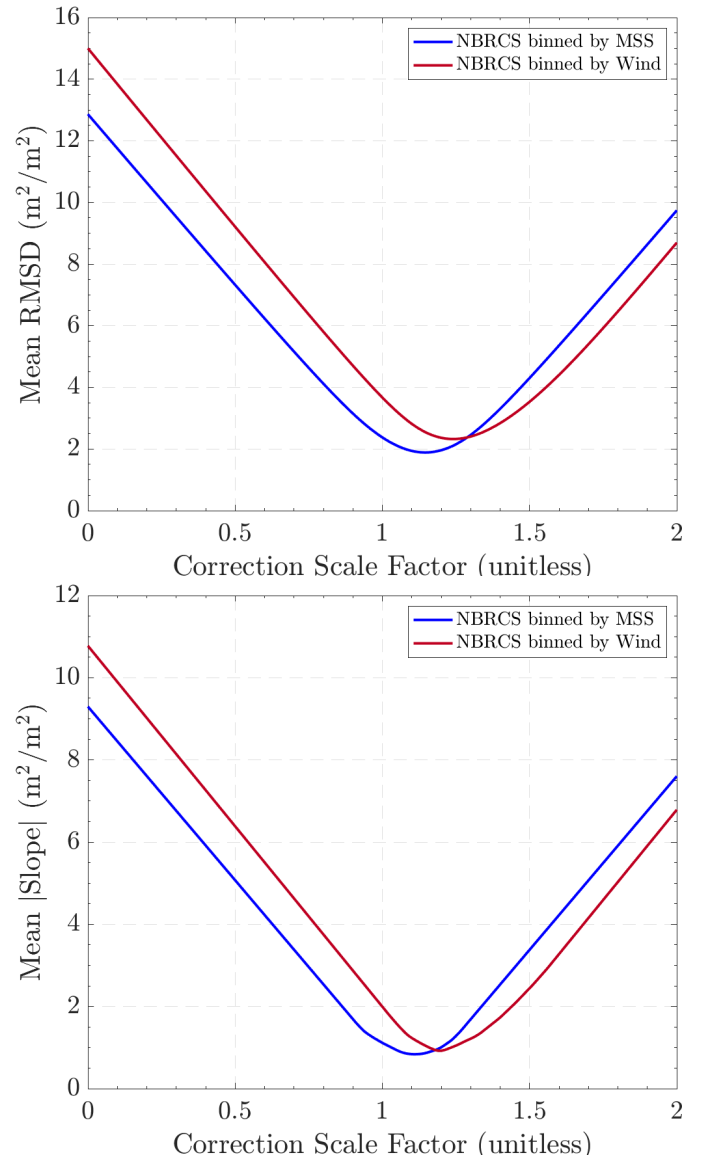


Fig. 8. Determination of empirical correction factor to theoretical noise floor correction curves. (Top) Mean RMSD error vs correction factor with respect to MSS and wind speed. (Bottom) Mean NBRCS slope magnitude vs correction factor with respect to MSS and wind speed.

$$\Gamma_{emp}(BR_{obs}) = \Gamma_{ref}(BR_{noise})X \quad (22)$$

Following, the correction to the CYGNSS level 0 observation noise floor is expressed as,

$$C_N^{corrected} = C_N \Gamma_{emp}(BR_{obs}) \quad (23)$$

where C_N is the raw level 0 noise counts, BR_{obs} is the per observation bin ratio, calculated as in Equation 19.

A single scaling factor (X) was determined for all nadir channels across all CYGNSS observatories using multiple NBRCS related performance criteria, including,

- 1) Minimize the relative variations of NBRCS under similar surface conditions across BR . Calculate the root mean square difference of mean NBRCS in narrow MSS and wind speed bins across bin ratio.

- 2) Maximize the consistency of the NBRCS under similar surface conditions across BR . Achieved by minimizing the $\frac{\Delta NBRCS}{\Delta BR}$ slope within narrow MSS and wind speed bins.

The mean RMSD and mean magnitude of the NBRCS slope over a range of correction scale factors (X) are shown in Figure 8. These RMSD and slope values are computed over a range of MSS and wind speed bins. In all cases, a clear minimum is evident. The optimal scale factor to the correction was determined by averaging the four minimums: RMSD(MSS), RMSD(wind), slope(MSS), slope(wind). This resulted in a final value of $X = 1.20$. A scale factor of $X < 1.0$ indicates the derived correction is too severe (that is, the derived correction over-estimates required correction at a given bin ratio), while $X > 1.0$ implies it is too light (that is, the derived correction under-estimates required correction at a given bin ratio), while a scale factor of 1.0 is the un-adjusted theoretical curve, Γ_{ref} .

The theoretical correction function and the empirically tuned theoretical correction function are both shown in Figure 7. It is important to note that the untuned theoretical correction is likely to contain errors due to interactions with downstream corrections in the CYGNSS v3.1 data products. Over the course of the development of the v3.1 algorithm, the optimal correction factor fluctuated between roughly 0.7 and 1.3, depending on independent changes being designed for other level 1 calibration terms (e.g. zenith and receive antennas, NBRCS area normalization, GPS Block de-biasing). Therefore, the optimal correction factor of 1.20 is valid only within the greater context of the CYGNSS v3.1 level calibration.

V. IMPACT AND CORRECTION OF DIGITAL SAMPLING ON CYGNSS TRANSMITTER POWER ESTIMATES

Recent iterations of the CYGNSS level 1 calibration algorithm (v3.0 and later) use real-time observations from the CYGNSS navigation antennas to estimate the EIRP of the GPS transmitters ([27], [28]). Like the nadir instrument channels, the zenith channels also operate in a fixed gain mode, with the bin ratio distributions having been previously presented in Figure 3(right).

A. Algorithm for Correcting Direct Channel Signal Levels

The CYGNSS zenith observations consist of integrated signal plus noise counts only, without a reference noise floor. This prohibits the application of the nadir noise floor correction to the zenith channel observations. Therefore, the observed zenith signal plus noise counts need to be corrected directly before a real-time EIRP estimate is formed [28]. Note that a decrease in the noise floor in the nadir calibration is equivalent to an opposite adjustment to the total signal plus noise counts ([29], [49]). As such, the reference digital sampling correction function can be adjusted for application to the zenith signal plus noise counts as,

$$\Lambda_{ref}^Z(BR_{noise}) = 1 + (1 - \Gamma_{ref}(BR_{noise})) \quad (24)$$

Like the nadir digital sampling correction, the zenith correction can also be optimized using empirical tuning factor(s) to

ensure consistency of the EIRP estimation as a function of natural bin ratio fluctuations. Due largely to the spread of zenith bin ratio PDFs with means under that associated with an ideal Gaussian distribution ($BR = 2.15$, see Table I), applying a single correction across all zenith observations was not possible and individual per-observatory corrections are required (25).

$$\Lambda_{emp}^Z(BR_{obs}^Z) = \Lambda_{ref}^Z(BR_{noise})Y(FM) \quad (25)$$

where BR_{obs}^Z is the observed bin ratio on the zenith channel and $Y(FM)$ is the per CYGNSS flight module (FM) empirical correction scale factor. The corrections are then applied to provide the corrected input signal plus noise counts needed in the EIRP estimation algorithm [28],

$$C_Z^{corrected} = C_Z \Lambda_{emp}^Z(BR_{obs}) \quad (26)$$

where C_Z is the uncorrected zenith direct signal plus noise counts for each CYGNSS observation and $C_Z^{corrected}$ is its corrected counterpart.

The per-FM zenith digital correction functions are shown in Figure 9. To better illustrate the need for an increased empirical correction factor ($Y(FM)$) as the \overline{BR} of the distributions decreases, the per-FM corrections are shown only between their 5% and 95% bin ratio limits, to better illustrate the correction values where the on-orbit observations occur for each CYGNSS FM. As a given zenith bin ratio distribution approaches that of an ideal Gaussian distribution with $\overline{BR} = 2.15$, only modest empirical adjustments are needed. An example of this is CYG05 requiring a scaling by a factor of 0.93 (i.e. a reduction of 7% relative to the untuned theoretical corrections) and thereby in near-perfect alignment with the reference zenith power correction curve shown in Figure 9. In contrast, as the bin ratio distribution diverges from this ideal reference PDF, a need for significantly increasing the correction ‘weights’ at a given bin ratio is evident. An example of this is CYG04 having a zenith $\overline{BR} = 1.01$ necessitating a scale of of 5.50.

B. Zenith Signal Correction Performance

The zenith signal digital corrections are evaluated with respect to the consistency of EIRP estimation across BR by each CYGNSS FM. An example of the before and after correction EIRP estimation across BR for CYGNSS FM 3 is shown in Figure 10. Before the digital sampling correction is applied there is a clear positive linear trend in the EIRP over a large range of BR (the bin ratio limits over which 95% of data occurs for a given FM). After the correction is applied the EIRP estimation is significantly more consistent (i.e. flatter) over the same BR range, reducing the maximum EIRP slopes by $\approx 92\%$. The pre-correction and post-correction estimated EIRP root-mean-square-difference (RMSD) presented on a per-FM basis are listed in Table III. EIRP is in units of Watts.

Parameter	FM 1	FM 2	FM 3	FM 4	FM 5	FM 6	FM 7	FM 8
Empirical Scale Factor, $Y(FM)$	3.15	4.25	1.35	5.50	0.93	4.40	2.40	3.45
Zenith BR Mean	1.17	0.99	1.64	1.01	1.64	1.35	1.25	1.16
EIRP RMSD, Uncorrected	113.97	123.88	96.76	101.19	72.69	130.30	101.17	102.86
EIRP RMSD, Corrected	23.91	28.99	20.91	16.18	22.83	23.40	24.21	19.57

TABLE III
SUMMARY OF CYGNSS ZENITH CHANNEL BIN RATIO DISTRIBUTIONS AND EIRP PRE-CORRECTION AND POST-CORRECTION PERFORMANCE.

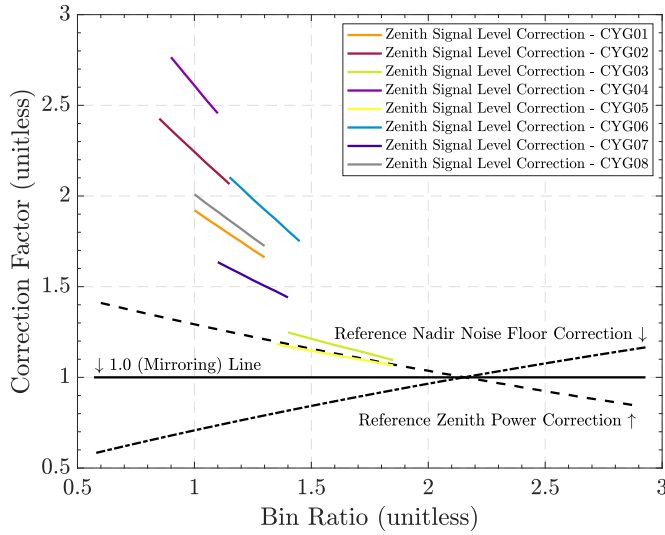


Fig. 9. CYGNSS FM specific zenith digital correction functions. Reference nadir correction is flipped around the 1.0 axis to accommodate the opposite signal plus noise counts correction. Scale factors are derived and applied to each FM individually. Corrections are shown for each FM over the 5%-95% range of observations where they are applied. This clearly demonstrates the deviation from the reference correction as the BR distribution shifts downward.

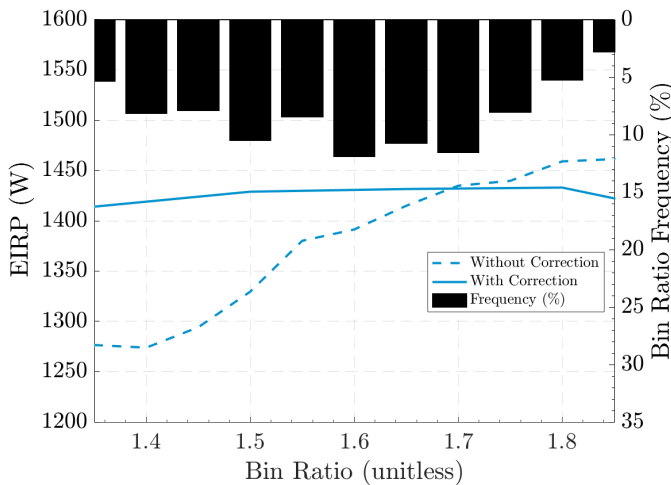


Fig. 10. Example zenith mean EIRP estimation over the BR range containing 95% of zenith observations for CYGNSS FM5. The pre-correction estimates (dotted line) clearly show a positive trend with BR that is largely mitigated with the digital sampling correction (solid line).

VI. ERROR ASSESSMENT OF CYGNSS DIGITAL SAMPLING CORRECTIONS

Initial analysis of the CYGNSS error budget was performed in [29], with the on-orbit performance assessed in [51] for the

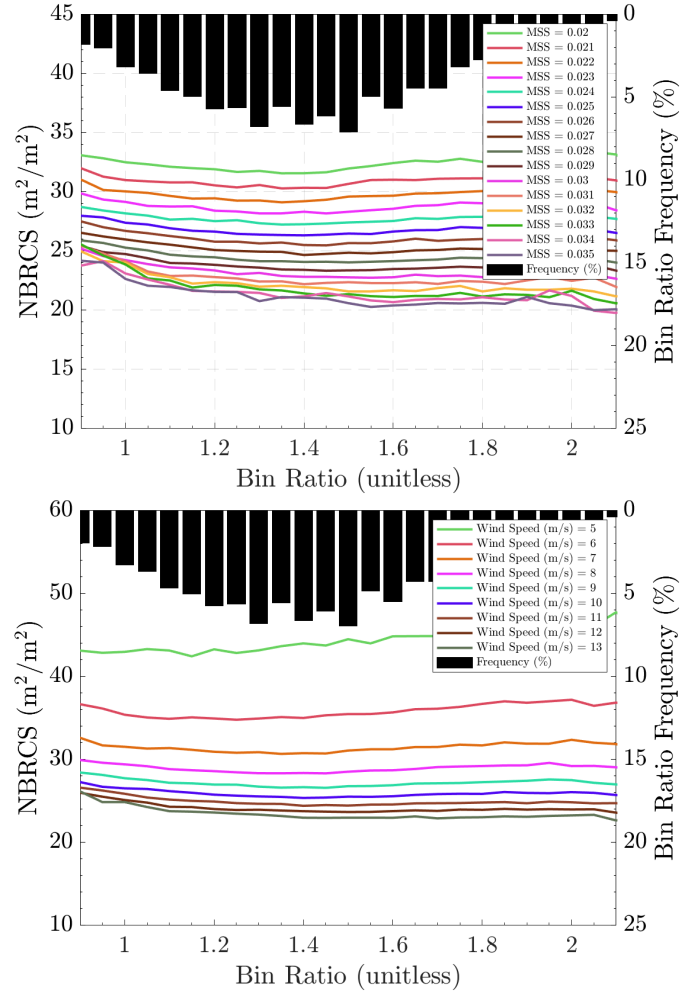


Fig. 11. NBRCS estimates vs science channel bin ratio over a range of ocean conditions with noise floor correction. (Top) With respect to surface MSS conditions (ref. WW3) and (Bottom) over a range of near surface wind conditions (ref. ECMWF)

level 1 NBRCS and in [41] for level 2 wind retrievals.

These studies were performed before the design and implementation of the above digital sampling corrections, which are expected to improve the previously published results.

This research is focused on the errors in the CYGNSS calibration due solely to digital sampling effects on the science and zenith antennas. The magnitude of these errors was assessed based on their impact to the NBRCS and EIRP estimations, respectively. A complete CYGNSS v3.1 calibration error analysis is being performed which includes all level 1 calibration parameters as part of a separate publication.

The corrections proposed here are based on the assumption

Surface Conditions	Uncorrected		Corrected	
	NBRCS RMSD (linear)	NBRCS Slope ($ \frac{\Delta NBRCS}{\Delta BR} $)	NBRCS RMSD (linear)	NBRCS Slope ($ \frac{\Delta NBRCS}{\Delta BR} $)
Wind Total (5-20 m/s)	12.90	9.34	2.79	1.48
Low Winds (5-7 m/s)	19.50	13.91	4.19	2.24
Medium Winds (7-12 m/s)	13.75	9.90	1.60	0.38
High Winds (12-20 m/s)	10.64	7.80	3.11	1.93
MSS Total (0.020-0.035)	12.86	9.30	1.89	0.84
Low MSS (0.020-0.025)	15.04	10.80	2.06	0.99
Medium MSS (0.025-0.030)	12.59	9.09	1.35	0.26
High MSS (0.030-0.035)	10.93	7.99	2.19	1.19

TABLE IV
SUMMARY OF CYGNSS PRE-CORRECTION AND POST-CORRECTION NBRCS ROOT MEAN SQUARE DEVIATIONS ACROSS WIND SPEED (REF. ECMWF) AND MSS (REF. WW3) SURFACE CONDITIONS.

that the BR is solely an internal instrument characteristic and it should not introduce undue uncertainty to the observed NBRCS or EIRP estimates. We would expect the same NBRCS estimates under the same surface conditions across all values of BR , as well as consistent EIRP observations independent of the instrument digital sampling distribution. The summary that follows is an analysis of the effectiveness of the digital sampling corrections as implemented on the CYGNSS v3.1 calibration algorithm.

Figure 5 clearly shows this is not the case without the digital sampling correction. With the above nadir and zenith digital sampling corrections, the CYGNSS NBRCS estimates as a function of BR and MSS and wind speed conditions significantly improve. The post-correction NBRCS vs BR performance is shown in Figure 11 across ranges of MSS and wind speed bins.

A summary of the results of this analysis is included in Table IV. These statistics are generated using all CYGNSS data from 2019, with temporal and spatial co-locations data from ECMWF (U10 wind speed) and WaveWatch III (L-band corrected MSS) used as the validation reference dataset.

VII. CONCLUSIONS AND DISCUSSION

This paper has described and quantified in detail the impact of fluctuating instrument noise levels on the digital sampling configuration of the CYGNSS instruments and the impact to the level 1 NBRCS estimates. A theoretical correction to the observed noise floor was derived based on the received 2-bit sampling distribution and fixed instrument front end gain settings. The theoretical noise floor correction was then adjusted empirically to minimize the errors and ensure consistency of the estimated NBRCS across a range of wind and MSS surface reference conditions obtained from global wind (ECMWF) and wave (WW3) models. Subsequently, an inverted version of the digital sampling correction was applied to the received navigation signal levels, and empirically adjusted for each CYGNSS observatory to minimize errors in the estimate of the GPS transmitter EIRP levels used in the level 1 calibration.

The resulting corrections were evaluated with 1-year of CYGNSS data, over a significant range of observed external noise fluctuations and shown to significantly improve the CYGNSS level 1 NBRCS calibration performance. The pre-correction NBRCS RMSD error due to noise induced BR variation was estimated as (mean) 12.90 between ECMWF

reference wind levels of 5-20 m/s, and (mean) 12.86 over Wavewatch III L-band corrected MSS values of 0.020-0.035. After the application of the digital sampling corrections the errors were reduced to (mean) 2.79 for the wind validation and 1.89 for the MSS surface reference. This represents a 78% and 85% improvement in RMSD estimation of the level 1 NBRCS, respectively.

REFERENCES

- [1] V.U. Zavorotny, S. Gleason, E. Cardellach and A. Camps, "Tutorial on remote sensing using GNSS bistatic radar of opportunity, IEEE Geosci. Remote Sens. Mag., vol. 2, no. 4, pp. 845, Dec. 2014.
- [2] S. Gleason, S. Lowe and V. Zavorotny (2009), Remote Sensing Using Bistatic GNSS Reflections, in GNSS Applications and Methods, S. Gleason and D. Gebre-Egziabher (editors), Artech House (Norwood, MA), 2009.
- [3] M. Martn-Neira, A passive reflectometry and interferometry system (PARIS): Application to ocean altimetry. ESA J. 1993, 17, 331355.
- [4] O. Eroglu, M. Kurum, D. Boyd and A. Gurbuz, "High Spatio-Temporal Resolution CYGNSS Soil Moisture Estimates Using Artificial Neural Networks," *Remote Sensing*, vol. 11, no. 19, p. 2272, 2019.
- [5] M. Clarizia, N. Pierdicca, F. Costantini and N. Floury, "Analysis of CYGNSS Data for Soil Moisture Retrieval," *IEEE Journal of Selected Topics in Applied Earth Observations and Remote Sensing*, vol. 12, no. 7, pp. 2227-2235, 2019.
- [6] C. Chew and E. Small, "Description of the UCAR/CU Soil Moisture Product," *Remote Sensing*, vol. 12, no. 10, p. 1558, 2020.
- [7] M. Al-Khaldi, J. Johnson, A. O'Brien, A. Balenzano and F. Mattia, "Time-Series Retrieval of Soil Moisture Using CYGNSS," *IEEE Transactions on Geoscience and Remote Sensing*, pp. 1-10, 2019.
- [8] H. Carreno-Luengo, G. Luzi and M. Crosetto, "Above-Ground Biomass Retrieval over Tropical Forests: A Novel GNSS-R Approach with CyGNSS," *Remote Sensing*, vol. 12, no. 9, p. 1368, 2020.
- [9] C. Chew, J. Reager and E. Small, "CYGNSS data map flood inundation during the 2017 Atlantic hurricane season," *Scientific Reports*, vol. 8, no. 1, 2018.
- [10] M. Morris, C. Chew, J. T. Reager, R. Shah and C. Zuffada, "A Novel Approach To Monitoring Wetland Dynamics Using CYGNSS: Everglades Case Study," *Remote Sensing of Environment*, 2019.
- [11] C. GerleinSafdi and C. Ruf, "A CYGNSSBased Algorithm for the Detection of Inland Waterbodies," *Geophysical Research Letters*, vol. 46, no. 21, pp. 12065-12072, 2019.
- [12] A. Warnock and C. Ruf, "Response to Variations in River Flowrate by a Spaceborne GNSS-R River Width Estimator," *Remote Sensing*, vol. 11, no. 20, p. 2450, 2019.
- [13] M. M. Al-Khaldi, J. T. Johnson, S. Gleason, C. Chew, C. Safdi, R. Shah and C. Zuffada, "Inland Water Body Mapping Using CYGNSS Coherence Detection," *IEEE Transactions on Geoscience and Remote Sensing (TGRS)*, 2020.
- [14] E. Loria, A. O'Brien, V. Zavorotny, B. Downs and C. Zuffada, "Analysis of Scattering Characteristics from Inland Bodies of Water Observed by CYGNSS," *Remote Sensing of Environment*, 2020.
- [15] E. Cardellach et al., "First Precise Spaceborne Sea Surface Altimetry With GNSS Reflected Signals," *IEEE Journal of Selected Topics in Applied Earth Observations and Remote Sensing*, vol. 13, pp. 102-112, 2020.

- [16] S. Gleason, "Space-based GNSS scatterometry: Ocean wind sensing using an empirically calibrated model, *IEEE Trans. Geosci. Remote Sens.*, vol. 51, no. 9, pp. 4853-4863, 2013.
- [17] M. Clarizia and C. Ruf, "On the Spatial Resolution of GNSS Reflectometry," *IEEE Geoscience and Remote Sensing Letters*, vol. 13, no. 8, pp. 1064-1068, 2016.
- [18] M. Clarizia, C. Ruf, P. Jales and C. Gommenginger, "Spaceborne GNSS-R Minimum Variance Wind Speed Estimator," *IEEE Transactions on Geoscience and Remote Sensing*, vol. 52, no. 11, pp. 6829-6843, 2014.
- [19] C. Ruf and R. Balasubramaniam, "Development of the CYGNSS Geophysical Model Function for Wind Speed," *IEEE Journal of Selected Topics in Applied Earth Observations and Remote Sensing*, vol. 12, no. 1, pp. 66-77, 2019.
- [20] M. Morris and C. Ruf, "Determining Tropical Cyclone Surface Wind Speed Structure and Intensity with the CYGNSS Satellite Constellation," *Journal of Applied Meteorology and Climatology*, vol. 56, no. 7, pp. 1847-1865, 2017.
- [21] M. M. Al-Khaldi, J. T. Johnson, Y. Kang, S. J. Katzberg, A. Bringer, E. Kubatko and D. Wood, "Track-based Cyclone Maximum Wind Retrievals Using The Cyclone Global Navigation Satellite System (CYGNSS) Mission Full DDMs," *IEEE Journal of Selected Topics in Applied Earth Observations and Remote Sensing (JSTARS)*, 2019.
- [22] M. M. Al-Khaldi, S. J. Katzberg, J. T. Johnson, Y. Kang and E. Kubatko, "Matched Filter Cyclone Maximum Wind Retrievals Using CYGNSS: Progress Update and Error Analysis," *IEEE Journal of Selected Topics in Applied Earth Observations and Remote Sensing (JSTARS)*, 2021.
- [23] V. Zavorotny and A. Voronovich, "Scattering of GPS signals from the ocean with wind remote sensing application," *IEEE Transactions on Geoscience and Remote Sensing*, vol. 38, no. 2, pp. 951-964, 2000.
- [24] A. G. Voronovich and V. U. Zavorotny, "Bistatic radar equation for signals of opportunity revisited," *IEEE Transactions on Geoscience and Remote Sensing*, vol. 56, No.3, pp. 1959-1968, April, 2018.
- [25] C.S. Ruf et al, "In-Orbit Performance of the Constellation of CYGNSS Hurricane Satellites," *Bull. Am. Meteorol. Soc.* 2019, 100, 20092023.
- [26] S. Gleason and C. Ruf, "Overview of the Delay Doppler Mapping Instrument (DDMI) for the cyclone global navigation satellite systems mission (CYGNSS)," *IEEE MTT-S International Microwave Symposium*, 2015.
- [27] T. Wang, C. S. Ruf, B. Block, D. S. McKague, and S. Gleason, Design and performance of a GPS constellation power monitor system for improved CYGNSS L1B calibration, *IEEE J. Sel. Topics Appl. Earth Observ. Remote Sens.*, vol. 12, no. 1, pp. 2636, Jan. 2019.
- [28] T. Wang et al., "Dynamic Calibration of GPS Effective Isotropic Radiated Power for GNSS-Reflectometry Earth Remote Sensing," *IEEE Trans. Geosci. Remote. Sens.*, doi: 10.1109/TGRS.2021.3070238.
- [29] S. Gleason, C.S. Ruf, M.P. Clarizia and A.J. O'Brien, "Calibration and Unwrapping of the Normalized Scattering Cross Section for the Cyclone Global Navigation Satellite System," *IEEE Trans. Geosci. Remote. Sens.* 2016, 54, pp. 2495-2509, doi:10.1109/tgrs.2015.2502245.
- [30] M. Unwin et al, "Spaceborne GNSS-reflectometry on TechDemoSat-1: Early mission operations and exploitation, *IEEE J. Sel. Topics Appl. Earth Observ. Remote Sens.*, vol. 9, no. 10, pp. 4525-4539, Oct. 2016.
- [31] S. Gleason, J. Johnson, C. Ruf and C. Bussy-Virat, "Characterizing Background Signals and Noise in Spaceborne GNSS Reflection Ocean Observations," in *IEEE Geoscience and Remote Sensing Letters*, vol. 17, no. 4, pp. 587-591, April 2020, doi: 10.1109/LGRS.2019.2926695.
- [32] G. Foti et al, "An Assessment of Non-geophysical Effects in Spaceborne GNSS Reflectometry Data From the UK TechDemoSat-1 Mission," *IEEE JSTARS*, Vol. 10, No. 7, July 2017.
- [33] R. Loh, "GPS Wide Area Augmentation System (WAAS)," *Journal of Navigation*, vol. 48, no. 2, pp. 180-191, 1995.
- [34] D. Stapelton, "GPS/Wide Area Augmentation System (WAAS) Final Approach Error Analysis," *Navigation*, vol. 50, no. 1, pp. 29-43, 2003.
- [35] R. Houghton, T. Strelch, C. Cluff and J. Valine, "Performance assessment of GPS augmentation systems," *IEEE Oceanic Engineering Society, OCEANS'98. Conference Proceedings* (Cat. No.98CH36259).
- [36] J.B. Hagen and D.T. Farley, Digital-correlation techniques in radio science, *Radio Sci.*, Vol. 8, p. 775-784, 1973, doi: 10.1029/RS008i008p00775
- [37] P. Misra and P. Enge, *Global Positioning System: Signals, Measurements, and Performance*. Ganga Jamuna Press, 2001. ISBN 0-9709544-0-9.
- [38] F.T. Ulaby and D.G. Long, *Microwave Radar and Radiometric Remote Sensing*: University Michigan Press: Ann Arbor, MI, USA, 2014
- [39] P. Steigenberger, S. Thielert and O. Montenbruck, "GPS and GLONASS Satellite Transmit Power: Update for IGS repro3," Technical Note, *WeBling*, Germany, 2019.
- [40] P. Daly, "Navstar GPS and GLONASS: global satellite navigation systems," *Electronics and Communications Engineering Journal*, vol. 5, no. 6, p. 349, 1993.
- [41] C. S. Ruf, S. Gleason, and D. S. McKague, Assessment of CYGNSS wind speed retrieval uncertainty, *IEEE J. Sel. Topics Appl. Earth Observ. Remote Sens.*, vol. 12, no. 1, pp. 8797, Jan. 2019.
- [42] P. Bechtold, P. Bauer, J.R. Bidlot, C. Cardinali, L. Magnusson, F. Prates and M. Rodwell, "Uncertainty in tropical winds," *Meteorology section of ECMWF Newsletter No. 134*, Winter 2012/13, pp. 3337.
- [43] M. Belmonte Rivas and A. Stoffelen, "Characterizing ERA-Interim and ERA5 surface wind biases using ASCAT," *Ocean Science*, vol. 15, no. 3, pp. 831-852, 2019.
- [44] The WAVEWATCH III Development Group (WW3DG), 2016: User manual and system documentation of WAVEWATCH III version 5.16. Tech. Note 329, NOAA/NWS/NCEP/MMAB, College Park, MD, USA, 326 pp.+ Appendices.
- [45] T. Wang, V. U. Zavorotny, J. Johnson, Y. Yi and C. Ruf, "Integration of Cygnss Wind and Wave Observations with the Wavewatch III Numerical Model," *IGARSS 2019 - 2019 IEEE International Geoscience and Remote Sensing Symposium*, 2019, pp. 8350-8353, doi: 10.1109/IGARSS.2019.8900481.
- [46] T. Wang et al., "Improvement of CYGNSS Level 1 Calibration Using Modeling and Measurements of Ocean Surface Mean Square Slope," *IGARSS 2020 - 2020 IEEE International Geoscience and Remote Sensing Symposium*, 2020, pp. 5909-5912, doi: 10.1109/IGARSS39084.2020.9323262.
- [47] M.P. Clarizia and C. S. Ruf, "Wind speed retrieval algorithm for the Cyclone Global Navigation Satellite System (CYGNSS) mission, *IEEE Trans. Geosci. Remote Sens.*, vol. 54, no. 8, pp. 4419-4432, Aug. 2016.
- [48] S. Soisuvarn, Z. Jelenak, F. Said, P.S. Chang and A. Egado, "The GNSS reflectometry response to the ocean surface winds and waves, *IEEE J. Sel. Topics Appl. Earth Observ. Remote Sens.*, vol. 9, no. 10, pp. 4678-4699, Oct. 2016.
- [49] S. Gleason, *CYGNSS Algorithm Theoretical Basis Documents, Level 1A and 1B*; University of Michigan: Ann Arbor, MI, USA, 2018.
- [50] B. F. C. Cooper, "Correlators with two-bit quantization," *Australian Journal of Physics*, vol. 23, no. 1, pp. 521-527, Aug. 1970.
- [51] S. Gleason, C. S. Ruf, A. J. O'Brien, and D. S. McKague, The CYGNSS level 1 calibration algorithm and error analysis based on on-orbit measurements, *IEEE J. Sel. Topics Appl. Earth Observ. Remote Sens.*, vol. 12, no. 1, pp. 3749, Jan. 2019.



Scott Gleason received the B.S. degree in electrical and computer engineering from the State University of New York at Buffalo, Buffalo, NY, USA, the M.S. degree in engineering from Stanford University, Stanford, CA, USA, and the Ph.D. degree in applied physics from the University of Surrey, Surrey, U.K., 1991, 1999 and 2007, respectively. He is a Project Scientist III with the University Corporation for Atmospheric Research, Boulder CO, USA. He is a Co-Investigator on the science team and Instrument Scientist for the NASA CYGNSS mission. He has worked in the areas of astronautics, remote sensing and global navigation satellite systems for more than 20 years, including at NASAs Goddard Space Flight Center, Stanfords GPS Laboratory, Surrey Satellite Technology Limited, Concordia University, and the National Oceanography Centre, Southampton.



Mohammad M. Al-Khaldi received the bachelors degree in electrical engineering from the American University of Sharjah, Sharjah, United Arab Emirates, in 2015, the M.S. degree in electrical engineering from Texas A&M University, College Station, TX, USA, in 2017, and the M.S. degree in electrical and computer engineering from The Ohio State University, Columbus, OH, USA, in 2019, where he finished his Ph.D. degree with the Department of Electrical and Computer Engineering and Electro-Science Laboratory in 2020. He is currently a post-

doctoral researcher at the University Corporation for Atmospheric Research in Boulder, Colorado. His research interests include applied electromagnetics, rough surface scattering, and spaceborne remote sensing



Tianlin Wang received the B.E. degree in electrical engineering from the East China University of Science and Technology, Shanghai, China, in 2009, the M.S. degree in radio physics from Fudan University, Shanghai, China, in 2012, and the M.S. and Ph.D. degrees in electrical engineering from the University of Michigan, Ann Arbor, MI, USA, in 2019 and 2021, respectively. His research work contributed to engineering calibration and geophysical retrieval for the Cyclone Global Navigation Satellite System NASA Earth Venture Mission. His research interests

include microwave remote sensing, microwave measurements, and radio frequency (RF) circuits. Dr. Wang is a member of Tau Beta Pi, Eta Kappa Nu, American Geophysical Union (AGU), and Institute of Navigation (ION) and an Early Career Member of Commission F of the U.S. National Committee (USNC) for the Union Radio Scientifique Internationale (URSI). He was a recipient of the 2018 IEEE Mikio Takagi Student Prize, the Outstanding Student Presentation Award at 2018 AGU Fall Meeting, the 2020 Richard F. and Eleanor A. Towner Prize for Distinguished Academic Achievement and Distinguished Leadership Award from the University of Michigan, and the 2021 Ernest K. Smith USNC-URSI Student Prize (Second Place).



Christopher S. Ruf received the B.A. degree in physics from Reed College, Portland, OR, and the Ph.D. degree in electrical and computer engineering from the University of Massachusetts at Amherst. He is currently Professor of atmospheric science and space engineering at the University of Michigan; and Principal Investigator of the Cyclone Global Navigation Satellite System NASA Earth Venture mission. He has worked previously at Intel Corporation, Hughes Space and Communication, the NASA Jet Propulsion Laboratory, and Penn State

University. His research interests include GNSS-R remote sensing, microwave radiometry, atmosphere and ocean geophysical retrieval algorithm development, and sensor technology development. Dr. Ruf is a member of the American Geophysical Union (AGU), the American Meteorological Society (AMS), and Commission F of the Union Radio Scientifique Internationale. He is former Editor-in-Chief of the IEEE Transactions on Geoscience and Remote Sensing and has served on the editorial boards of Radio Science and the Journal of Atmospheric and Oceanic Technology. He has been the recipient of four NASA Certificates of Recognition and seven NASA Group Achievement Awards, as well as the 1997 TGRS Best Paper Award, the 1999 IEEE Resnik Technical Field Award, the 2006 IGARSS Best Paper Award, and the 2014 IEEE GRSS-S Outstanding Service Award.



Darren S. McKague received the Ph.D. degree in Astrophysical, Planetary, and Atmospheric Sciences from the University of Colorado, Boulder, in 2001. He is an Associate Research Scientist in the Department of Climate and Space Sciences and Engineering at the University of Michigan. Prior to working for Michigan, he worked as a systems engineer for Ball Aerospace and for Raytheon, and as a research scientist at Colorado State University. His work has focused on remote sensing with emphases on the development of space-borne microwave remote

sensing hardware, microwave remote sensor calibration techniques, and on mathematical inversion techniques for geophysical retrievals. His experience with remote sensing hardware includes systems engineering for several advanced passive and active instrument concepts and the design of the calibration subsystem on the Global Precipitation Mission (GPM) Microwave Imager (GMI) as well as the development of calibration and inter-calibration techniques for the GPM constellation. His algorithm experience includes the development of a near-real time algorithm for the joint retrieval of water vapor profiles, temperature profiles, cloud liquid water path, and surface emissivity for the Advanced Microwave Sounding Unit (AMSU) at Colorado State University, and the development of the precipitation rate, precipitation type, sea ice, and sea surface wind direction algorithms for the risk reduction phase of the Conical scanning Microwave Imager/Sounder (CMIS).



Anthony Russel received the B.S. degree in computer science engineering from Michigan State University, East Lansing, MI, USA, in 2014. He is a member of the engineering staff with the Space Physics Research Laboratory, College of Engineering, University of Michigan, Ann Arbor, MI, USA. His primary engineering activities involve algorithm development and large-scale data processing as a member of the Science Operations Center for the CYGNSS mission.